

# On the effect of a low viscosity asthenosphere on the temporal change of the geoid—A challenge for future gravity missions

Gabriele Marquart<sup>a,\*</sup>, Bernhard Steinberger<sup>b</sup>, Karen Niehuus<sup>c</sup>

<sup>a</sup> *SRON and Institute of Earth Science, University of Utrecht, The Netherlands*

<sup>b</sup> *Institute for Frontier Research in Earth Evolution, Yokosuka, Japan*

<sup>c</sup> *Institute of Meteorology and Geophysics, J.W. Goethe University, Frankfurt, Germany*

Accepted 18 April 2005

## Abstract

New satellite technology to measure changes in the Earth's gravity field gives new possibilities to detect layers of low viscosity inside the Earth. We used density models for the Earth mantle based on slab history as well as on tomography and fitted the viscosity by comparison of predicted gravity to the new CHAMP gravity model. We first confirm that the fit to the observed geoid is insensitive to the presence of a low viscosity anomaly in the upper mantle as long as the layer is thin ( $\sim 200$  km) and the viscosity reduction is less than two orders of magnitude. Then we investigated the temporal change in geoid by comparing two stages of slablet sinking based on subduction history or by advection of tomography derived densities and compared the spectra of the geoid change for cases with and without a low viscosity layer, but about equal fit to the observed geoid. The presence of a low viscosity layer causes relaxation at smaller wavelength and thus leads to a spectrum with relatively stronger power in higher modes and a peak around degrees 5 and 6. Comparing the spectra to the expected degree resolution for GRACE data for a 5 years mission duration shows a weak possibility to detect changes in the Earth's gravity field due to large scale mantle circulation, provided that other causes of geoid changes can be taken into account with sufficient accuracy. A discrimination between the two viscosity cases, however, demands a new generation of gravity field observing satellites.

© 2005 Elsevier Ltd. All rights reserved.

**Keywords:** Geoid; Geoid anomalies; Mantle dynamics; Mantle viscosity; GRACE satellite mission

\* Corresponding author. Tel.: +31 30 253 5142; fax: +31 30 253 5030.

E-mail address: [marquart@geo.uu.nl](mailto:marquart@geo.uu.nl) (G. Marquart).

## 1. Introduction

Density variations in the Earth's mantle in excess of a purely radial distribution cause solid state viscous flow of mantle rocks which leads to plate tectonics, volcanism and earthquakes. To understand quantities such as flow pattern, dynamic topography, or the state of stress transmitted to the base of the lithosphere, the viscosity profile of the mantle has to be known. From postglacial rebound observations (e.g. Mitrovica, 1996), as well as laboratory studies on mantle rocks under high temperature and pressure conditions an average value of  $10^{21}$  Pa s is well established for the upper part of the mantle (e.g. Ranalli, 1995). However, postglacial rebound studies mainly probe continental shield regions and may not give representative values on a global scale at least for the upper 250 km, and laboratory data suffer from the unknown amount of water present in olivine which has a pronounced effect on the viscosity (Hirth and Kohlstedt, 1996).

In several studies during the last two decades it was attempted to determine the viscosity profile within the Earth from a combination of internal density data sets, in most cases deduced from tomography, and gravity potential coefficients. The long wavelength equilibrium figure of the Earth, the geoid, is characterized by undulations on the order of a few tens of meters. This shape of the Earth can be well explained by density variations throughout the mantle mainly due to plate subduction, and the dynamic response of a viscous Earth. The dynamic response causes boundary mass anomalies (i.e. dynamic topography) which add to the internal density anomalies and the sum can be positive or negative for the same internal driving density anomalies depending on the viscosity. In most of these studies the viscous Earth was modeled as a number of self-gravitating spherical shells for which the equations of motion can be solved analytically for a radially stratified viscosity (e.g. Richards and Hager, 1984).

Various types of modeling included petrological phase boundaries in the mantle, surface plate velocities (e.g. Ricard et al., 1989; Forte et al., 1991) or mineral physics (e.g. Steinberger and Calderwood, 2001; Forte and Mitrovica, 2001) to derive density from seismic tomography. The various authors generally agree that the viscosity increases by 1–2 orders of magnitudes throughout the mantle (e.g. Lithgow-Bertelloni and Richards, 1998). Steinberger and Calderwood (2001), however, found a gradual increase by almost a factor of 1000. Whether the increase is predominately gradual or stepwise from the upper to the lower mantle is still debated.

Internal density distributions have been deduced from a slab sinking model taking into account the crustal creation rate for the last 100 Ma from ocean floor age data (e.g. Ricard et al., 1993), or from seismic s- or p-wave tomography. Tomography gives the spatial distribution of anomalies of seismic s- or p-wave velocities in comparison to a radial standard Earth model. A principal problem in all these studies is the uncertainty in the relationship between seismic velocity and density  $\frac{\delta \rho}{\rho} = \frac{\partial \ln \rho}{\partial \ln v} \frac{\delta v}{v}$ . Laboratory studies on mantle rocks give a roughly constant conversion or scaling factor  $\frac{\partial \ln \rho}{\partial \ln v}$  between 0.2 and 0.4 assuming only thermally induced density variations (Karato, 1993). However, an increasing number of more recent studies (e.g. Forte and Perry, 2000; Marquart, 2005) favor a depth dependent scaling factor, based on the assumption of mineral phase changes in the mantle and possible chemical differentiation.

For studying the dynamics of plate motions, in particular due to the transmission of stress from the mantle to the lithosphere, the viscosity in the uppermost mantle below the lithosphere (i.e. at a depth range between 100 and 300 km) is of primary interest. While for continents, at least in shield areas, deeply situated high viscosity roots have been proposed in agreement with seismological findings, for oceanic and active continental areas an effective decoupling zone below the plates is very likely. Indications for low viscosities below 100 km beneath the Pacific ocean have been reported by e.g. Wieland and Knopoff

(1982) using Rayleigh wave dispersion data. This is also in agreement with laboratory data for dunite at mantle temperatures and stresses between 1 and 10 MPa for which viscosities as low as  $10^{17}$  Pa s have been extrapolated if water is present (Chopra and Paterson, 1984). These findings support a viscosity drop by 1–2 orders of magnitudes (relative to a value of  $10^{21}$  Pa s) below 100 km depth, at least outside continental shield regions. However, it has been shown before and will be demonstrated here that the resolution for such a low-viscosity asthenospheric layer is poor when modeling the observed geoid. On the other hand, since such a layer has a pronounced effect on the relaxation of the Earth due to changes in loading, the temporal variations of the geoid are sensitive to the presence of a low viscosity decoupling layer. Cadek and Fleitout (2003) showed that the fit to the geoid can be further improved by allowing lateral viscosity variations. The viscosity field that results from their optimization makes intuitively sense (i.e. low viscosity under ridges, high under continents). Here we do not wish to include lateral viscosity variations in order to keep things simple.

The GRACE satellite project has a designed mission duration of 5 years and will for the first time allow to investigate the temporal variations of the Earth gravity potential field with high resolution. Here we investigate the effect of a low viscosity layer in the upper mantle on temporal variations of the geoid and the possibility to discriminate between different models with GRACE observation data. We used two different mantle density models, one based on a slab sinking model (Ricard et al., 1993) and one on a recent tomography model (s20rts, Ritsema and van Heijst, 2000), and two alternative viscosity profiles, one with and one without a low viscosity asthenosphere, both providing a good fit to the observed (static) CHAMP geoid (Reigber et al., 2002).

Since the model based on the time evolution of sinking slablets is of more idealized nature, one may prefer a tomography model as a better representation of observations and closer to reality. However, the amplitudes of tomography models are strongly affected by parameterization, damping and irregular data coverage. Especially around the mantle transition zone (400–800 km) coverage is poor (e.g. Ritsema et al., 2004). Because of these tradeoffs, we consider both models here.

## 2. The static models—fitting the observed geoid

Our analysis is based on deriving geoid kernels (or mantle response functions) for a given viscosity depth profile. The kernels have been calculated with a code developed by Ricard (e.g. Ricard et al., 1993) for an incompressible mantle and self-consistent “incompressible” gravity.

For the mechanical boundary at the surface we used a free slip condition. It has been shown (e.g. Hager and Richards, 1989) that the long wavelength features of the geoid can well be reproduced with this simple condition and a laterally uniform lithosphere as long as the lithosphere viscosity is in the range of 10–100 times the upper mantle viscosity. It should be noted that this condition does not successfully reproduce surface plate motion. The problem of simulating observed plate motion or incorporating it in the model approach has led to ambiguous results in a number of studies. Karpychev and Fleitout (1996) tested various methods, such as weak zones, force balance, and imposed plate motion, to include the effect of plate tectonics in the predicted geoid and conceived the latter method by far the best way. However, if this approach leads to an improved fit of the modeled geoid to the observed one is still an open question. Cadek and Fleitout (1999) achieved a geoid variance reduction of 75% for these kinematic boundary conditions and partial layering, which is similar to fits achieved under free-slip upper boundary conditions. Other studies however (e.g. Ricard et al., 1989; Thoraval and Richards, 1997) could not find

an improved fit to the observed geoid. The fit was comparable to that obtained for no slip condition, but not as good as found for free slip. In a newer study by [Zhong and Davies \(1999\)](#) the authors consider the inclusion of plate motion as a surface condition meaningful only in conjunction with laterally strong and weak zones in the lithosphere. In this study we decided to use free slip conditions for a kernel approach with merely vertical viscosity variations.

The kernels describe the geoid produced in a viscous Earth by a unit mass anomaly of a given zonal spherical harmonic at a given depth. The mathematical expression to derive the kernels  $G_l(r, \mu(r))$  itself is lengthy and will not be repeated here, it can be found in [Richards and Hager \(1984\)](#) and [Ricard et al. \(1984\)](#). The spherical harmonic coefficients of the model geoid  $N_{lm}^{c,s}$  are found by multiplying the kernels with the density contrast  $\delta\rho_{lm}^{c,s}$

$$N_{lm}^{c,s} = \frac{4\pi\gamma a}{g(2l+1)} \int_{\text{CMB}}^a G_l(r, \mu(r)) \delta\rho_{lm}^{c,s}(r) dr \quad (1)$$

$\gamma$  is the gravitational constant,  $g$  the gravity acceleration of a spherical reference Earth comprising a constant density mantle and core,  $a$  the Earth radius, CMB the core radius. The (fully normalized) modeled geoid can then directly be computed from the  $N_{lm}^{c,s}$  by a spherical harmonic synthesis and compared to observations. A measure for the fit between the modeled  $N_{lm}^{\text{mod}}$  and observed geoid  $N_{lm}^{\text{obs}}$  is given by the variance reduction  $\Phi$

$$\Phi = \left[ 1 - \left( \frac{\sum_{l=0}^{l_{\text{max}}} \sum_{m=0}^l (N_{lm}^{\text{obs}} - N_{lm}^{\text{mod}})^2}{\sum_{l=0}^{l_{\text{max}}} \sum_{m=0}^l (N_{lm}^{\text{obs}})^2} \right) \times 100 \right]. \quad (2)$$

The variance reduction may be interpreted as the percentage of observed data satisfying the model predictions.

Although the geoid kernels include the effect of the dynamic topography and kernels for dynamic topography can easily be formulated, dynamic topography can hardly be used as an additional constraint. The contribution of the dynamic topography to the observed topography on Earth is only poorly known, since the contribution of the isostatically compensated crust and lithosphere is difficult to discern and uncertainties are large and on the order of the signal itself ([Panasyuk and Hager, 2000](#)). The amplitude of dynamic topography may be as high as 2 km ([Panasyuk and Hager, 2000](#)), but much lower amplitudes around 0.5 km ([Kaban, personal communication](#)) have also been proposed.

The driving density distributions in the mantle have been deduced from a slab subduction history model (SM) and a s-wave tomography model (TM). The slab sinking model for the last 100 Ma was derived by Lithgow-Bertelloni ([Ricard et al., 1993](#)) defining subduction arcs and velocities over time and assuming vertical material sinkers (slablets) at successive time intervals. Subduction velocity was reduced by a factor 4.5 in the lower mantle, the excess density was set constant and later determined by the best fit to the geoid, values are normally around 75 kg/m<sup>3</sup> for a plate thickness of 100 km. For the tomography model we used the model s20rts by [Ritsema and van Heijst \(2000\)](#) which has proved to allow the best fit to the observed geoid compared to other recent tomographic models ([Marquart, 2005](#)). The s-wave to density conversion factor was assumed to be depth dependent and found by the fit between modeled and observed geoid, as explained further down. Only for the results shown in [Fig. 1](#) we used a constant conversion factor of 0.24. This value was found by optimizing the fit for s20rts for a constant scaling factor. The mantle was divided into 20 layers of equal thickness of 145 km and the densities were calculated at mid-layer depth for each layer and expanded in spherical harmonics up to degree and order 20 and truncated for degree and order 15 with a cosine taper applied over the five additional higher harmonics. For geoid and

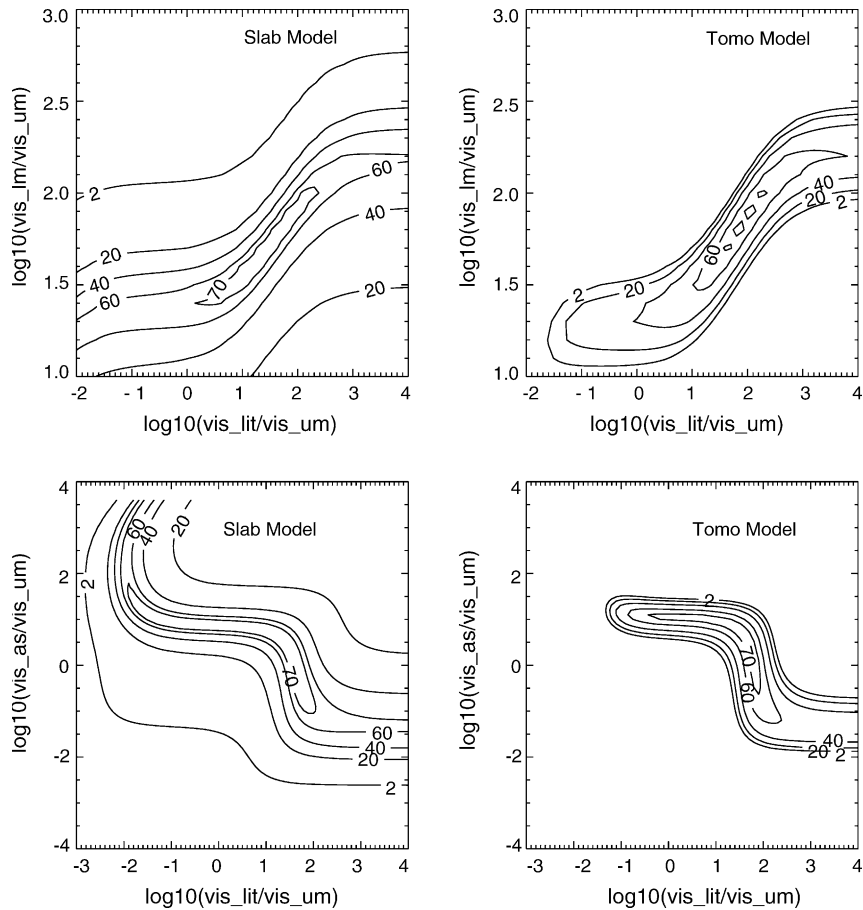


Fig. 1. Isolines of  $\Phi$  (variance reduction) for the CHAMP geoid and a modeled geoid based on a slab and a tomographic density model for spherical harmonic degrees between 2 and 15. In the upper two diagrams a three layer mantle model was assumed and the viscosity of the lithosphere and the lower mantle was varied in relation to the upper mantle viscosity. The lower diagrams show the effect of an additional asthenospheric layer between 100 and 280 km; here the lower mantle viscosity was fixed to  $40 \times 10^{21}$  Pa s. For the tomography model, the scaling factor is 0.24.

gravity we used the CHAMP gravity model (Reigber et al., 2002) reduced by the hydrostatic reference figure of the Earth (Lambeck, 1988) and also truncated for spherical harmonics  $L > 15$  with a cosine taper. The Champ gravity model was used since its error degree variances as a measure for the power of the error are slightly smaller than those of the EGM96 gravity model (Amos and Featherstone, 2003) up to  $L = 32$ . However, the small differences between various recent gravity models are not essential for our study.

For the viscous Earth model we assumed for simplicity in the first instance a four layer model as given in Table 1. Already with a simple three layer model where the asthenosphere has the same viscosity as the upper mantle, a good fit to the observed geoid can be obtained for both the SM and the TM. To demonstrate this well known fact, we show in Fig. 1 (two upper diagrams) isolines of  $\Phi$  obtained by varying lithosphere and lower mantle viscosity. A variance reduction to better than 70% is found if the

Table 1

Depth of isoviscous Earth layers used for the fitting in Fig. 1

Layer	Depth (km)
Lithosphere	0–100
Asthenosphere	100–280
Mid mantle	280–670
Lower mantle	670–2900

viscosity of the lithosphere is by a factor 10–100 higher than the upper mantle viscosity and the viscosity of the lower mantle is higher by 30 to 100 times. Including an additional asthenospheric layer, and a viscosity in the lower mantle of  $40 \times 10^{21}$  Pa s, results in  $\Phi$  values given in the two lower diagrams in Fig. 1. For realistic values of viscosity in the lithosphere, the ratio of asthenospheric to upper mantle viscosity cannot be resolved and lies between 0.06 and 10. This long known dilemma was the reason for us to look for temporal variations of the geoid with respect to asthenosphere viscosity. We also found that the densities derived from the slab model allow a better fit to the observations with this simple approach than the densities based on tomography. This is presumably due to the use of a constant scaling factor for the fitting in Fig. 1, assuming all seismic wave speed anomalies are of merely thermal origin.

In the next step we set up a six layer model with depth variable scaling factor for the tomography derived densities and did a Monte Carlo search for two viscosity and scaling factor profiles which allow an equally good fit to the observed geoid. For the Monte Carlo search first a regular search grid was established between certain upper and lower limits for viscosity and scaling factor and then random picks were made around grid points of already high variance reduction. Altogether about  $10^6$  different combinations of viscosity and scaling factor profiles were calculated. In Table 2 the layering of our model and the upper and lower limits for viscosity ( $\mu_u$ ,  $\mu_l$ ) and conversion factor ( $c_u$ ,  $c_l$ ) are given.

In the first parameter set the viscosity in the three upper mantle layers was held constant and in the second case a parameter space with a low-viscosity asthenosphere was searched. The first parameter set was obtained by a search for the highest variance reduction to the observed geoid for a combination of the slab model and the tomography model. To get that we determined the minimum

$$\min_i \left\langle \left( \frac{|\Phi_i - \Phi_{\max,T}|}{\Phi_{\max,T}} \right) + \left( \frac{|\Phi_i - \Phi_{\max,S}|}{\Phi_{\max,S}} \right) \right\rangle \quad (3)$$

Table 2

Depth of Earth layers and viscosity and scaling factor bounds used for the fitting of model M1 and M3 in Fig. 2

Layer	Depth (km)	$\mu_l$ (Pa s)	$\mu_u$ (Pa s)	$c_l$	$c_u$
Lithosphere	0–100	$10^{22}$	$10^{23}$	0	0.2
Upper mantle					
Asthenosphere	100–280	$10^{19}$	$5 \times 10^{21}$	0	0.2
Sub-asthenosphere	280–410	$10^{19}$	$5 \times 10^{21}$	0.1	0.4
Transition zone	410–670	$10^{19}$	$5 \times 10^{21}$	0.1	0.4
Lower mantle					
Upper part	670–1150	$5 \times 10^{21}$	$5 \times 10^{22}$	0.2	0.4
Lower part	1150–2800	$10^{22}$	$10^{23}$	0.2	0.4



The indexes T and S indicate the tomography and the slab model,  $\Phi_{\max,S}$  and  $\Phi_{\max,T}$  are the maximum variance reduction obtained for the tomography and the slab model, respectively, and the index  $i$  is over all Monte Carlo parameter combinations.

This setup gives correlation values between modeled and observed geoid of  $\sim 83\%$  for the tomography derived density and  $\sim 88\%$  for the slab density model and variance reductions of 70 and 77%, respectively. For the second parameter set (see Table 2) we allowed three independent layers in the upper mantle. It turned out that there exists also a tradeoff between the viscosities in the asthenosphere and the upper mantle layer beneath, in the way that the correlation to the observed geoid varies only by about 1% for a variation of the asthenosphere viscosity over 1.5 magnitudes. In fact, since in the second case the parameter space is larger we achieved for the best parameter sets a slightly better fit than in the first case (the variance reduction for the slab model remained the same, for the tomography-based model a maximum value of 72% was obtained).

A variance reduction of 70% or more is assumed to represent a model compatible with the long-wavelength geoid (e.g. Cadek and van den Berg, 1998). Variance reduction is generally better for slab based density models. However, with the synthetic tomography model smean (Becker and Boschi, 2002), obtained by averaging over a number of tomography models and more mantle layers Steinberger and Holme (2002) got a variance reduction of up to 81%.

For the tomography model alone the best parameter set even indicated a weak increase in viscosity for the asthenosphere layer. However, the best fit for a combination of both, tomography and slab model, in the sense of Eq. (3) points to a reduction in asthenospheric viscosity. Since here we are mainly interested in the effect of a low viscosity asthenosphere, we choose a parameter set which gives a slightly worse fit than the best one in sense of Eq. (3), but which still has nearly the same correlation value as for the constant viscosity upper mantle case and allows a viscosity reduction by a factor of 0.015 in the asthenosphere. The viscosity and scaling factor profiles which we used are shown in Fig. 2. It should be mentioned however, that keeping the scaling factor profile from the first parameter set and only adding a low viscosity layer to the viscosity profile would have resulted in a strongly reduced fit to the static geoid with the second parameter set.

We did not explicitly specify a low viscosity layer at the core-mantle boundary, since we assumed for the model approach already a free slip boundary. We are aware that with a low-viscosity layer near the CMB results might be slightly different, since in this case CMB topography is smaller, which also gives a contribution to the geoid at very long wavelengths. However, to keep the model simple we did not include an additional layer.

Our viscosity profile for case M1 resembles very much the profiles found by Ricard et al. (1993) and Corrieu et al. (1995) obtained by similar studies to predict the long wavelength geoid. Viscosity model M3 is more similar to profiles resulting from some studies predicting postglacial rebound signatures (e.g. Lambeck et al., 1996). It is also in agreement with the assumption that the viscosity in the asthenosphere may be reduced due to the geotherm being close to the melting curve, and possibly partial melting. In the transition zone, a reduction of viscosity may be due to the presence of water (e.g. Kavner, 2003).

Note that the conversion factor does not change value at  $\sim 280$  km for model M3 and at  $\sim 410$  km for model M1. This was not prescribed, but an outcome of our fitting procedure. The scaling factor for model set M3 (dashed line in Fig. 2) is low down to 410 km. While depth variations of the scaling factor can well be explained by phase changes of different mineralogical mantle constituents, even in case of perfect mixing, such a low scaling value implies that the existence of a low-viscosity asthenosphere is only consistent with the gravity field observations if seismic wave speed velocities in this part of the

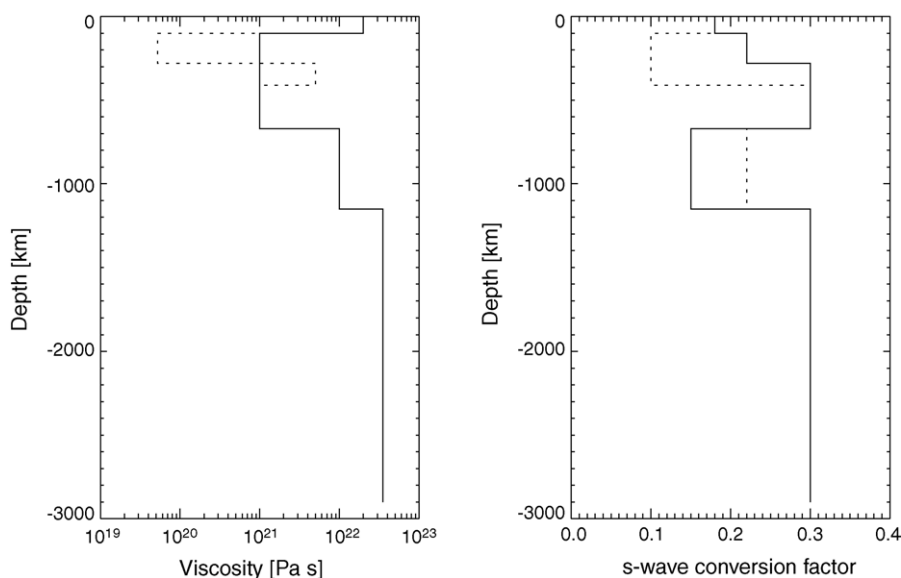


Fig. 2. Viscosity and s-wave to density scaling factor profiles used for modeling temporal variations of the geoid. The solid line gives a constant viscosity for the upper mantle (model M1) and the dashed line gives an alternative model with a low asthenospheric viscosity (model M3).

mantle are at least partly due to chemical differentiation in the uppermost mantle, such as a chemically distinct “tectosphere”. It is also noteworthy that for both models the conversion factor below the mantle transition zone, in the uppermost lower mantle, is small. Since in the same region also seismic velocity variations are generally weak, its low scaling factor reduces the effect on the density field even more, separating upper and lower mantle density anomalies.

In Fig. 3 the CHAMP geoid with respect to a hydrostatic Earth is compared to the modeled geoids for the slab (model SM1) and the tomography derived densities (model TM1) for  $L = 2–15$ . The synthetic geoids for the parameter setup M3 are not shown, since they are nearly identical to those given here. The tomography based data better represent the geoid high over the W-Pacific, but the slab model better matches the negative anomalies over northern Eurasia and N-America. The general good agreement between the two modeled and the observed present-day geoid is due to the fact that the geoid is dominated by the longest wavelengths of density anomalies which have a high correlation between the tomography and the slab model, but for higher degrees the correlation becomes poor (e.g. Becker and Boschi, 2002).

To illustrate the different density distributions for the slab history and tomography-based models we show in Fig. 4 the degree power spectra ( $\sum_{m=0}^l \Delta N_{lm}^{c2} + \Delta N_{lm}^{s2}$ )<sup>1/2</sup> of the density distribution for both models at different depth. The density field derived from slab history (Fig. 4, upper part) is mainly concentrated in the lower mantle. This is caused by the reduced sinking velocity below the transition zone which results in increasing accumulation of slab material. Since slabs are relatively thin, spectral energy increases towards higher degrees. On the contrary, tomography based density contrasts are concentrated in the upper and lowermost mantle with a rather equal energy distribution over all degrees, beside a preference for degree 2 anomalies mainly below 1600 km. Additionally a peak around degrees 5 and 6 can be found at various depths. Even though the overall density effect appears to be much stronger for the



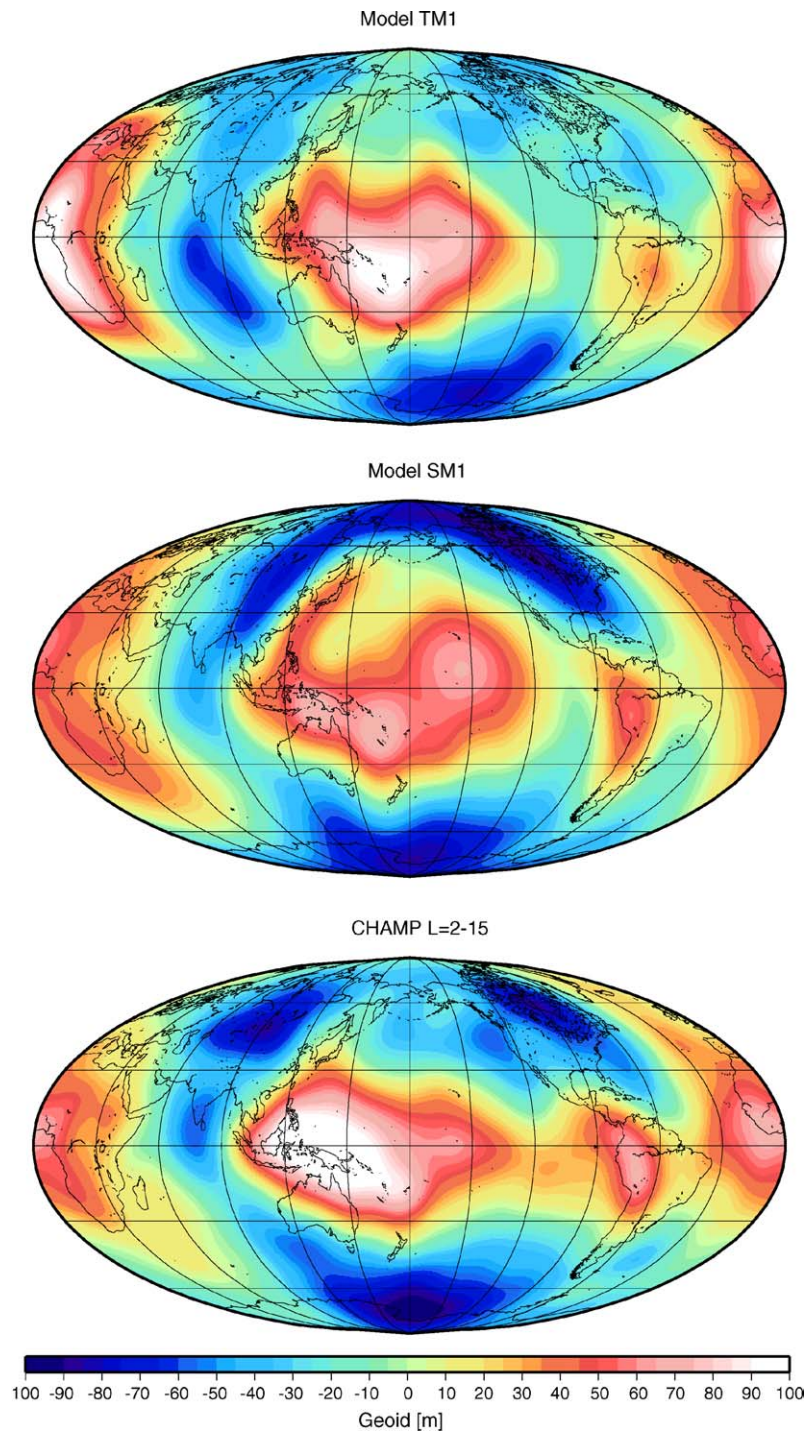


Fig. 3. Modeled geoids as produced by the tomography (TM1, top) and slab derived density (SM1, center) distribution for the Earth model M1 (see Fig. 2) in comparison to the hydrostatic CHAMP geoid (bottom).

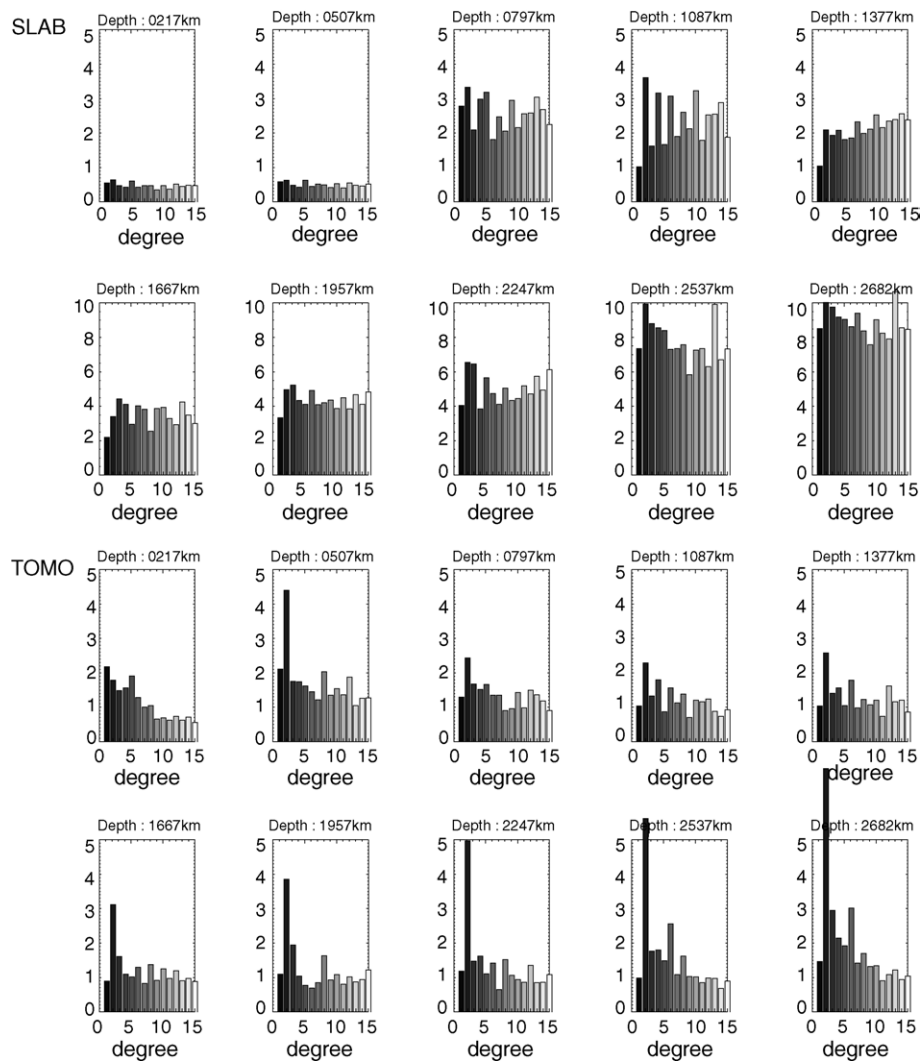


Fig. 4. Power spectra of the density anomalies at various depths in the mantle based on slablet sinking (top) and the tomography model s20rts (Ritsema and van Heijst, 2000). Note the different scaling of the lower mantle anomalies for the slab model.

slab-based model (note the larger range at the y-axis below 1377 km), the spectral energy for degrees 2 and 3 are comparable. Since these modes have the main effect on the resulting geoid, also the maximum geoid amplitudes are of the same order, as seen in Fig. 3.

### 3. Temporal changes of the geoid

For the two Earth parameter sets and the two mantle density models we then derived the temporal change in geoid. Our approach here is based on the assumption that convection in the Earth mantle is time dependent. This is mainly motivated by the fact that the main driving force for convection, plate

subduction, is not steady state, nor is seafloor spreading. While any mass distribution in the Earth's mantle results in an instantaneous convective response (described by the solution of the Navier–Stokes equation), the time dependence arises due to advection and diffusion of density related heat or chemical composition. Here we investigate advected density anomalies over a time span of 1 Ma, but neglect diffusion. This is motivated by the fact that for length scales larger than 100 km and flow velocities in excess of 1 cm/a the Peclet Number, describing the relative importance of advective to diffusive transport, becomes large enough to neglect diffusion. If we assume time dependence, we can expect that density changes due to diffusion are small compared to those due to advection everywhere except in the thermal boundary layers. Thus, if within the time span considered only a small fraction of the total mantle is advected into or out of thermal boundary layers, which is certainly the case for 1 Ma, diffusion can be ignored.

For the parameter set based on the slab subduction history model we compared the present geoid to the geoid 1 Ma back in time (1 Ma less of subduction, i.e. 1 Ma less of sinking time for the slabs). We consider that material subducted during the last 1 Ma is “added” at the top and material which reached the CMB is “removed” from the model (i.e. by thermal or chemical assimilation). For the tomography derived model we advected the related densities backward in time (Steinberger and O’Connell, 1997) for 1 Ma, using mantle flow vectors computed with present-day plate motion boundary condition, and other model assumptions as for the fit to the observed geoid. As discussed earlier, imposing plate motion boundary conditions would not allow us to improve the fit to the geoid, however, it is most appropriate for computing the actual flow and advection.

In Figs. 5 and 6 we show the temporal geoid change based on the slab densities and the tomography derived densities for the Earth model M1 (top) and M3 (bottom). The four resulting temporal variations of the long wavelength geoid are quite different. A general finding from all models is that the change in geoid has relatively more power in smaller wavelengths than the geoid itself. This is even more pronounced for the tomography-based models. To illustrate this finding we have plotted in Fig. 7 the degree power spectra (definition see above), normalized by each maximum, for the observed geoid and for our four modeled cases of temporal geoid change.

All models show a concentration of spectral energy around degrees 5–6 and 10. For the slab density model, however, the spectrum of the change in geoid is still quite similar to the observed geoid spectrum, indicating that low degrees of high power also change more rapidly and that the temporal change in geoid is approximately proportional to the static amplitude, while for the tomography derived density model the spectrum is nearly flat between degrees 5 and 15, indicating that in this spectral range all modes change with about the same rate.

The explanation for the differences of the spectra of geoid changes between the two density models is most likely due to temporal changes in upper mantle convection. Upper mantle density variations for all degrees considered are relatively strong in the tomography-based model (Fig. 4, lower part) and lead presumably to a time varying flow field. The related geoid changes are only weakly suppressed due to their shallow origin. For the slab history based model high spectral energy of the density anomalies is present in the deep mantle (Fig. 4, upper part), but the high viscosity allows only slow changes of the flow field and the possible effect on the geoid changes is mainly attenuated since the place of origin is deep.

To illustrate this point somewhat further, we discuss the density changes in a particular area together with the geoid kernels. The slope of the geoid kernels changes the sign a few times with depth, as a consequence, small differences in the depth of density anomalies between the slab and the tomography model have a pronounced effect on the predicted geoid change. Since for shorter wavelengths the agreement between the two model geoids becomes less good, this leads to the rather different temporal geoid changes. To

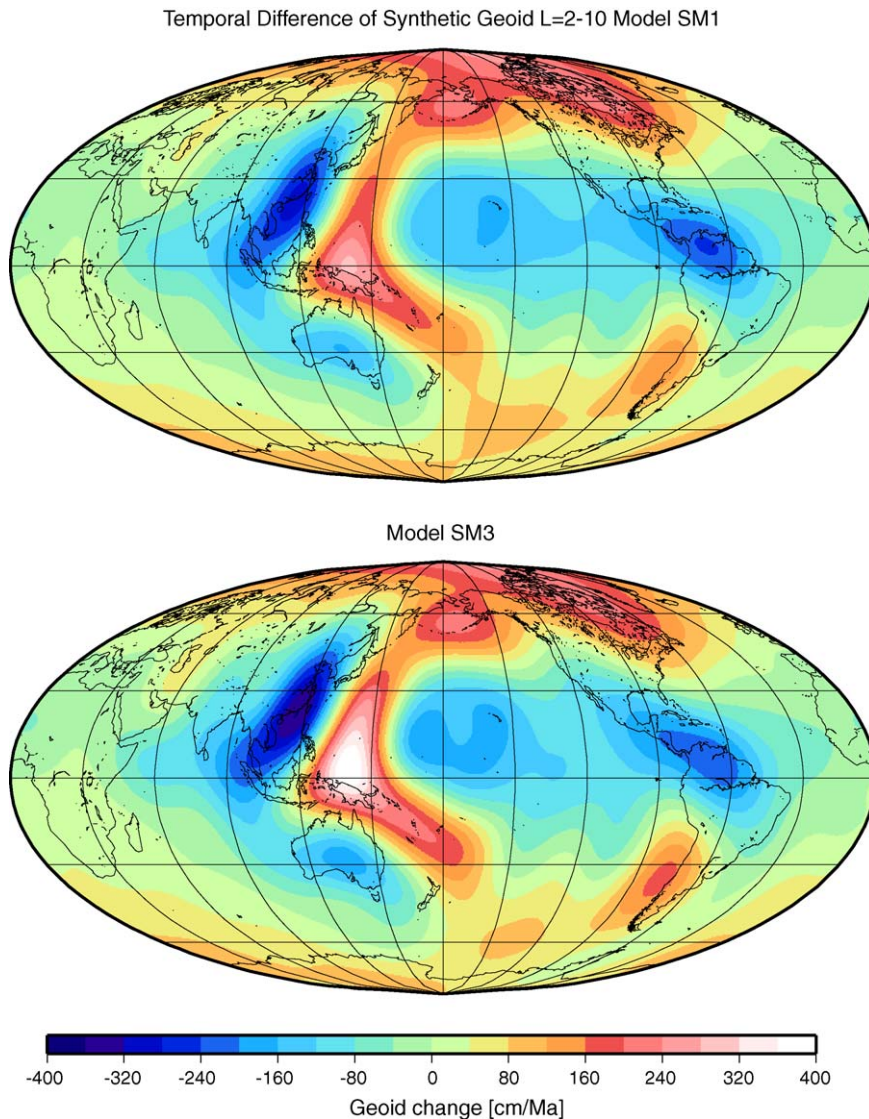


Fig. 5. Temporal geoid change in cm/Ma based on the slab subduction model (Ricard et al., 1993) and Earth parameters according to setup M1 (top) and M3 (bottom).

illustrate the relation between density change and predicted geoid change in more detail we show in Fig. 8 the temporal density change with depth averaged over a part of the East China Sea between  $25^{\circ}$  and  $34^{\circ}$ N and  $125^{\circ}$  and  $134^{\circ}$ E. This area has relatively strong subduction related signal. The profiles for the temporal density changes are given on the right side of Fig. 8, solid line for slab history model related densities changes and dotted line for densities changed due to advection of the tomography related densities. The advection was based on the viscosity profile M3 (see Fig. 2) for which we also show the geoid kernels (used in Eq. (1)) for degrees  $l = 2, 4, 8, 12$  (left side of Fig. 8). The slab density change profile is nearly zero in the upper 1000 km, indication that no change in lateral slab position was included in the model for



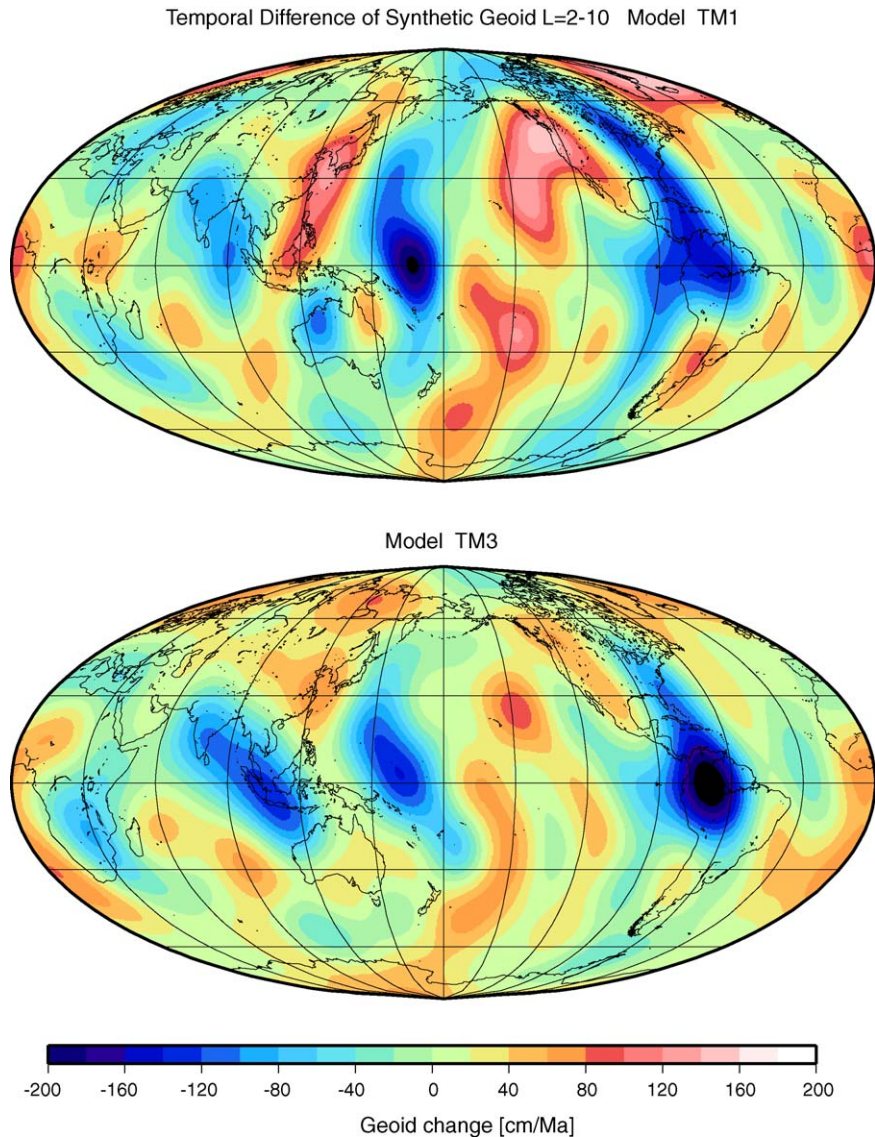


Fig. 6. Temporal geoid change in cm/Ma based on the tomography model s20rts (Ritsema and van Heijst, 2000) and Earth parameters according to setup M1 (top) and M3 (bottom).

the last 1 Ma. The main density changes arise from cumulation of slab material in the lowermost mantle. The tomography derived density changes are slightly negative in the uppermost mantle, where the ‘loss’ in density is presumably related to a change in slab subduction geometry over time due to trench roll back. In the mid mantle clear temporal density changes occur in the tomography related density model. We believe that this is caused by interactions of the slab with the mantle transition zone, reflected in the tomography model. Also for the tomography based density model the strongest density changes are in the deep mantle indicating accumulation of slab material close to the core-mantle boundary. If we compare

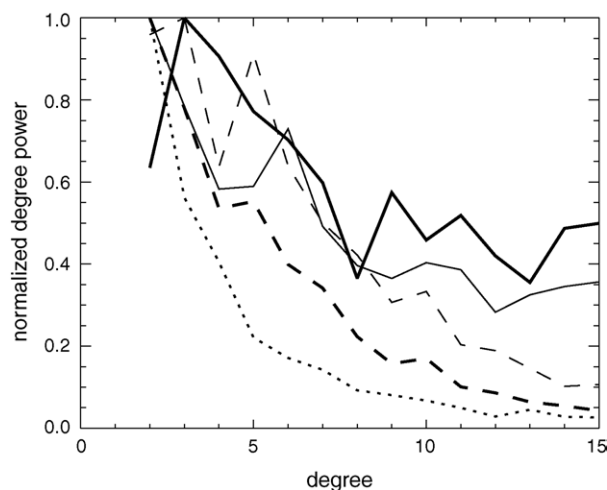


Fig. 7. Degree power spectra of the geoid changes in comparison to the spectrum of the observed geoid (dotted line) to illustrate the difference in spectral energy loss with increasing degree. For comparison all spectra are normalized by their maxima, respectively. Dashed lines are for the models with slab history based densities and solid lines for the tomography derived densities. The thick lines refer to viscosity profile M1 and thin lines to M3 (see Fig. 2).

the density change profiles to the geoid kernels it becomes obvious that the dominating effect for the slab case arises for degree 2 from the lower mantle density accumulation, leading to a negative change of geoid anomaly in this particular area. For the tomography-based models the effect due to deeply situated density changes is less, instead the density changes close to the mantle transition zone produce a positive geoid anomaly for various harmonic degrees, since all geoid kernel functions peak between 500 and 800 km. What we have discussed for this particular area is also true for many other subduction regions and provides also the explanation for the relatively stronger power in higher modes of the power spectra derived from the tomography models (Fig. 9, upper two plots) in comparison to the spectra based on the slab densities (Fig. 9, lower two plots).

The slab history based models (Fig. 5, SM1 and SM3) are, as could be expected, dominated by the subduction zone distribution, mainly due to the accumulation of slab material in the lower mantle roughly beneath the subduction zone. The geoid rises at the subduction and over the attached plate and subsides over the overriding plate. Nearly no change of the geoid is found in the Atlantic and over the African plate. If we compare the slab history based model (Fig. 5) with the one based on tomography (Fig. 6) we find that all models predict a rise of the geoid in the eastern US and the North Atlantic and in the Antarctic region, and a subsidence in Central America and around India. Stronger disagreement is observed in the central Pacific, here mantle flow related to the Hawaiian Plume and the Pacific Superswell can also be expected to produce a changing density field in time and to cause a change in geoid. For the tomography related density model (Fig. 6) we predict a clear temporal rise of the geoid for Hawaii but an uncertain result for the SW Pacific. These plume signals cannot be expected in a purely slab driven model (Fig. 5) since plume related density anomalies are simply not present.

The slab driven model (Fig. 5) produced a pronounced rise of the geoid seaward of the subduction zones; this effect is also visible in the tomography-based models (Fig. 6) but to a much lesser degree. This pattern is easy to understand by recalling the shape of the geoid kernels. Following the geoid kernels from



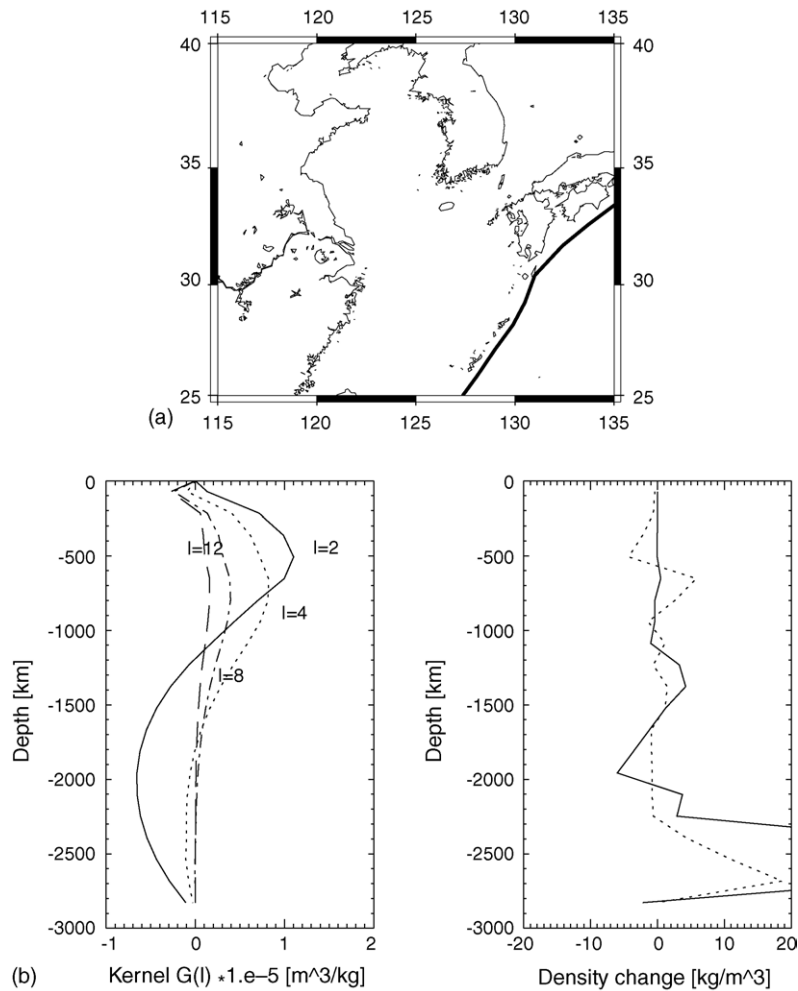


Fig. 8. Comparison of temporal changes of density with depth (right side) to geoid kernels with depth for degrees 2–12 (left side) (note that the factor  $\frac{4\pi\gamma a}{g(2l+1)}$  is included in the kernels). Temporal density changes are shown for the tomography based densities (right, dotted line) and for the slab history derived densities (right, solid line). Density changes were averaged over an area in the East China Sea (see small figure above) between 25° and 34°N and 125° and 134°E. The density change profiles show for both cases an accumulation of dense material at the lowermost mantle, giving rise to geoid anomalies of degree 2. Tomography based density changes in the upper-lower mantle transition cause higher harmonic geoid anomalies.

a depth of  $\sim 100$  km to bottom, the values first increase, then decrease and increase again. For sinking slabs with trench rollback one should expect the following: close to the trench, where the slab is still at shallow depth, a positive geoid change should occur, further away a negative change and even further away a weak positive change. Thus stripes of changing sign are to be expected. This is exactly what we found in the western Pacific in all of our models; due to obvious reasons more pronounced for the slab derived densities. In regions with strong “vertical” density anomalies, expected for the “superplumes” or for nearly stationary vertical subduction, the change in geoid is difficult to predict since here the exact density distribution and changes in density distribution over depth are crucial. Since plate subduction

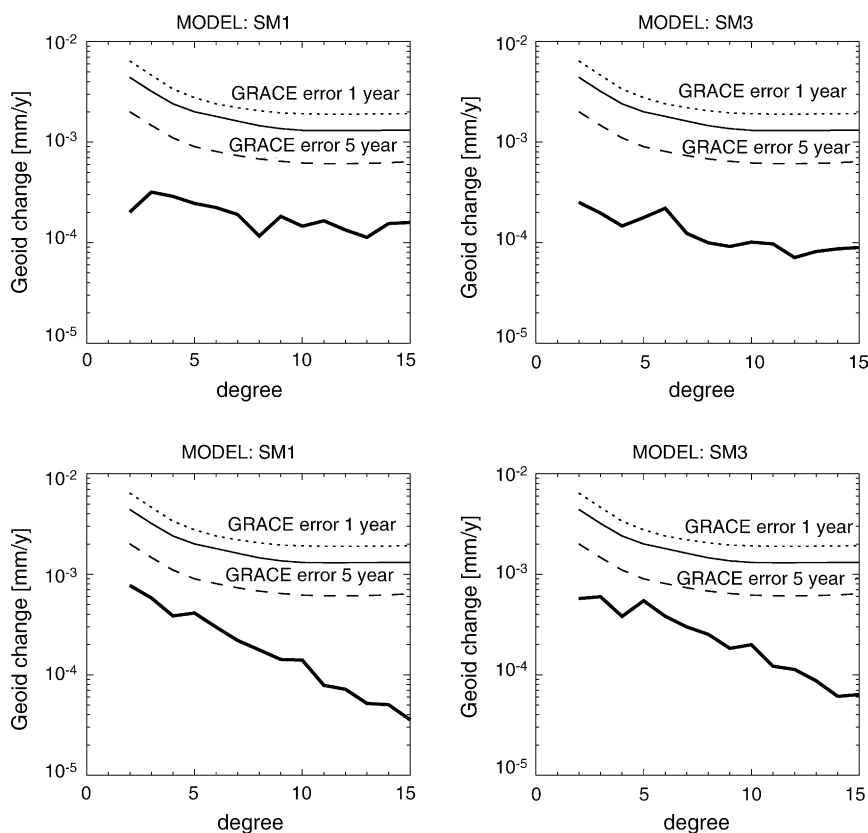


Fig. 9. Spectra of the geoid change for a model with (right side) and without (left side) low viscosity layer at 200 km depth; upper graphs are related to densities derived from tomography, lower graphs from a slab sinking model. All other parameters are as shown in Fig. 2. Also shown is the degree resolution expected for a 1 and 5 year GRACE satellite mission duration following Kaufmann (2002) (thin solid and dashed line) and for 1 year flight duration accuracy according to Wahr et al. (1998) (dotted line).

provides both major density anomalies and a dominant driving force for mantle flow, the exact places where the subducted plates are in time has a major effect on the temporal change of the geoid. This might explain the different locations of the subduction related highs in geoid change in the slab and the tomography driven models.

This leads to the important question, which features are robust? Robust features can be accepted for Central and South America, where also a rather good agreement between slab and tomography models is found (Steinberger, 2000). Here all our models show a negative temporal change in the geoid in the northern segment of the Andean subduction zone and a positive one further south. The same pattern and magnitude were also found by Steinberger and O'Connell (2002) for a model with different density anomalies and viscosity profile. In areas of trench rollback, as in the Northeastern (and partly Western) Pacific, at least the pattern of temporal change of the geoid can be predicted. Especially for the North American continent a tendency for these trench roll back related stripes can be found. In the central Pacific and also in central-southern Africa, "superplume" related density changes are very likely and will have an effect on the geoid change, however, the sign is not obvious.

The second point to address is the effect of a low viscosity layer at asthenosphere depth. In the slab-based model the existence of a low viscosity zone (SM3, Fig. 5 bottom) has only a minor effect on the temporal change of the geoid with slightly enhanced anomalies in the western Pacific. For the tomography-based model the effect of a low viscosity layer is stronger. Anomalies related to plumes as for Hawaii or to the African and south Pacific superplume are reduced since the low viscosity layer decouples flow from the deeper mantle and reduces the effect of dynamic topography. Anomalies of shallow origin as for the section of the Nazca plate with low angle subduction are enhanced.

Since there are no significant differences in the spatial domain for cases with and without a low-viscosity asthenosphere, which would help to resolve such a layer, we investigated the spectral distribution of energy. To study this in more detail we have plotted the degree spectrum for all four models (Fig. 9) again, but now with the actual scale and in comparison to the anticipated degree resolution for the GRACE satellite mission, assuming a 1 and 5 years mission duration (Kaufmann, 2002; Wahr et al., 1998).

For both density cases we found that the existence of a low viscosity asthenosphere concentrates spectral energy around degrees 5 or 6. From this we can conclude that in case the spectral energy distribution could be measured with enough accuracy, indications for such a layer might be detected, which is not resolvable without considering temporal changes. However, it should be emphasized that our models can only give a rough estimate of possible geoid changes caused by mantle processes. The density scaling used for the tomography-based model (Fig. 2, left figure) has been found by fitting the static geoid, which is dominated by very low degree terms. For these terms a merely radial scaling law seems to be sufficient. For smaller scale density variations the scaling law varies for different regions (e.g. Deschamps et al., 2002) depending on the dominance of thermal or chemical effects. This in turn has a strong influence on the style of upper mantle flow and its temporal variations. Furthermore, a viscosity profile based on a static geoid fit, only constraints relative viscosity variations with depth, absolute values and hence rate of change are estimated from postglacial rebound, but are uncertain by a factor of  $\sim 1.7$  (Mitrovica, 1996). Additionally, lateral variations in viscosity might enhance temporal changes in mantle flow. Under these considerations our models might give a conservative estimate.

But are these small effects likely to be observed by new satellite technology? The amplitudes of the temporal change in geoid are not very different for all models and are on the order of 2–4 m/Ma (Figs. 5 and 6). To measure these small changes by satellite observations is certainly a challenge. The GRACE satellite mission is planned for a time span of 5 years. Over this time interval the predicted maximum change in geoid due to dynamic processes of the solid Earth is only about 0.02 mm. Comparing our modeled geoid changes to the expected resolution of the GRACE satellite mission, we find that the spectral energy of the temporal geoid change is less than the anticipated limits of accuracy for a 5 year flight duration (Fig. 9). However, the definite accuracy of the GRACE measurements is still a matter of debate. In Fig. 9 we also show two different pre-flight estimates of accuracy for the 1 year flight duration (Kaufmann, 2002; Wahr et al., 1998), which already have a considerable offset. It should also be mentioned that the accuracy after more than 1 year of data recovery for GRACE is still more than one order of magnitude worse than the predicted level (Schwintzer, 2004, personal communication). But even if the effect would be within the accuracy limits of the satellite observations, the crucial point is, if this effect can be separated from others, as those due to ocean circulation, redistribution of water and biological masses, or massive volcanic processes and glacial deloading. However, to have an estimate about the magnitude of the effects of large scale mantle flow on the temporal change of the geoid and its spatial distribution, might also put constraints on other models of any contributions to temporal gravity changes.

## Acknowledgments

We thank Yanick Ricard for giving us his mantle transfer function program and the slab subduction history data set. Peter Schwintzer gave us access to the CHAMP potential field coefficients. The comments of Harro Schmeling and two anonymous reviewers helped to improve the original manuscript. Most figures were produced with the GMT graphic software (Wessel and Smith, 1995). This work was supported by a research grant of the Deutsche Forschungsgemeinschaft to one of us (KN).

## References

- Amos, M.J., Featherstone, W.E., 2003. Comparisons of recent global geopotential models with terrestrial gravity field data over New Zealand and Australia. *Geomat. Res. Austr.* 79, 1–20.
- Becker, T.W., Boschi, L., 2002. A comparison of tomographic and geodynamic mantle models. *Geochem. Geophys. Geosyst.* 3 2001G000168.
- Cadek, O., van den Berg, A.P., 1998. Radial profiles of temperature and viscosity in the Earth's mantle inferred from the geoid and lateral seismic structure. *Earth Planet. Sci. Lett.* 164, 607–615.
- Cadek, O., Fleitout, L., 1999. A global geoid model with imposed plate velocities and partial layering. *J. Geophys. Res.* 104, 29055–29075.
- Cadek, O., Fleitout, L., 2003. Effects of lateral viscosity variations in the top 300 km on geoid, dynamic topography and lithospheric stresses. *Geophys. J. Int.* 152, 566–580.
- Chopra, P.N., Paterson, M.S., 1984. The role of water in the deformation of dunite. *J. Geophys. Res.* 89, 7861–7876.
- Corrieu, V., Thoraval, C., Ricard, Y., 1995. Mantle dynamics and geoid Green functions. *Geophys. J. Int.* 120, 512–523.
- Deschamps, F., Trampert, J., Snieder, R., 2002. Anomalies of temperature and iron in the uppermost mantle inferred from gravity data and tomographic models. *Phys. Earth Planet. Int.* 84 (129), 245–364.
- Forte, A.M., Mitrovica, J.X., 2001. Deep-mantle high-viscosity flow and thermochemical structure inferred from seismic and geodynamic data. *Nature* 410, 1049–1056.
- Forte, A.M., Peltier, W.R., Dziewonski, A.M., 1991. Inferences of mantle viscosity from tectonic plate velocities. *Geophys. Res. Lett.* 18, 1747–1750.
- Forte, A.M., Perry, H.K.C., 2000. Seismic-geodynamic constraints on mantle flow: implications for layered convection, mantle viscosity, and seismic anisotropy in the deep mantle. In *Earth's Deep Interior*, *Geophys. Monogr. Ser.* vol. 117, AGU, Washington, DC, 2–26.
- Hager, B.H., Richards, M.A., 1989. Long-wavelength variations in Earth's geoid: physical models and dynamical implications. *Phil. Trans. R. Soc. Lond., A.* 328, 209–327.
- Hirth, G., Kohlstedt, D.L., 1996. Water in the oceanic upper mantle: implications for rheology, melt extraction and the evolution of the lithosphere. *Earth Planet. Sci. Lett.* 144, 93–108.
- Karato, S., 1993. Importance of anelasticity in the interpretation of seismic tomography. *Geophys. Res. Lett.* 20, 1623–1626.
- Karpychev, M., Fleitout, L., 1996. Simple considerations on forces driving plate motion and on the plate-tectonic contribution to the long-wavelength geoid. *Geophys. J. Int.* 127, 268–282.
- Kaufmann, G., 2002. Predictions of secular geoid changes from late pleistocene and holocene Antarctic ice-mass imbalance. *Geophys. J. Int.* 148, 340–347.
- Kavner, A., 2003. Elasticity and strength of hydrous ringwoodite at high pressure. *Earth Planet. Sci. Lett.* 214, 645–654.
- Lambeck, K., 1988. *Geophysical Geodesy, The Slow Deformation of the Earth*. Clarendon Press, Oxford, 718 pp.
- Lambeck, K., Johnston, P., Smither, C., Nakada, M., 1996. Glacial rebound of the British Isles, III: constraints on mantle viscosity. *Geophys. J. Int.* 125, 340–354.
- Lithgow-Bertelloni, C., Richards, M.A., 1998. Dynamics of cenozoic and mesozoic plate motions. *Rev. Geophys.* 36, 27–78.
- Marquart, 2005. Inferring mantle viscosity and s-wave-density conversion factor from new seismic tomography and geoid data. *Geophys. J. Int.*, submitted for publication.
- Mitrovica, J.X., 1996. Haskell [1935] revisited. *J. Geophys. Res.* 101, 555–569.

- Panasjuk, S.V., Hager, B.H., 2000. Models of isostatic and dynamic topography, geoid anomalies, and their uncertainties. *J. Geophys. Res.* 105, 28199–28209.
- Ranalli, G., 1995. *Rheology of the Earth*. Chapman and Hall, London.
- Reigber, Ch., Balmino, G., Schwintzer, P., Biancale, R., Bode, A., Lemoine, J.-M., Koenig, R., Loyer, S., Neumayer, H., Marty, J.-C., Barthelmes, F., Perosanz, F., Zhu, S.Y., 2002. A high quality global gravity field model from CHAMP GPS tracking data and accelerometry (EIGEN-1S). *Geophys. Res. Lett.* 29 (14), DOI: 10.1029/2002GL015064.
- Ricard, Y., Fleitout, L., Froidevaux, C., 1984. Geoid heights and lithospheric stresses for a dynamic Earth. *Ann. Geophys.* 2, 267–286.
- Ricard, Y., Richards, M., Lithgow-Bertelloni, C., Le Stunff, Y., 1993. A geodynamic model of mantle density heterogeneity 98, 21895–21909.
- Ricard, Y., Vigny, C., Froidevaux, C., 1989. Mantle heterogeneities, geoid and plate motion: a Monte Carlo inversion. *J. Geophys. Res.* 94, 13739–13754.
- Richards, M.A., Hager, B.H., 1984. Geoid anomalies in a dynamic Earth. *J. Geophys. Res.* 89, 5987–6002.
- Ritsema, J., van Heijst, H.J., 2000. Seismic imaging of structural heterogeneity in Earth's mantle: evidence for large-scale mantle flow. *Sci. Progr.* 83, 243–259.
- Ritsema, J., van Heijst, H.J., Woodhouse, J.H., 2004. Global transition zone tomography. *J. Geophys. Res.* 109 (B2), B02302 DOI: 10.1029/2003JB002610.
- Steinberger, B., O'Connell, R.J., 1997. Changes of the Earth's rotation axis owing to advection of mantle density heterogeneities. *Nature* 387, 169–173.
- Steinberger, B., 2000. Slabs in the lower mantle—results of dynamic modelling compared with tomographic images and the geoid. *Phys. Earth Planet. Inter.* 118, 241–257.
- Steinberger, B., Calderwood, A., 2001. Models of viscous flow in the Earth's mantle with constraints from mineral physics and surface observations. Abstract "International workshop on mantle convection and lithosphere dynamics", Aussois, France.
- Steinberger, B., O'Connell, R.J., 2002. The convective mantle flow signal in rates of true polar wander. In: Mitrovica, J.X., Vermeersen, L.L.A. (Eds.), *Ice Sheets, Sea Level and the Dynamic Earth*, *Geodyn. Ser.*, vol. 29. AGU, Washington, DC, pp. 233–256.
- Steinberger, B., Holme, R., 2002. Mantle flow models with core mantle boundary constraints. Abstract, SEDI2002, 'Geophysical and geochemical evolution of the deep Earth', Granlibakken, Tahoe City, CA, USA, 22–26 July 2002.
- Thoraval, C., Richards, M.A., 1997. The geoid constraint in global geodynamics: viscosity structure, mantle heterogeneity models and boundary conditions. *Geophys. J. Int.* 131, 1–8.
- Wahr, J., Molenaar, M., Bryan, F., 1998. Time variability of the Earth's gravity field: hydrological and oceanic effects and their possible detection using GRACE. *J. Geophys. Res.* 103, 30205–30229.
- Wessel, P., Smith, W.H.F., 1995. New version of the generic mapping tools released. *EOS Trans. AGU* 76, 329.
- Wieland, E., Knopoff, L., 1982. Dispersion of very long-period Rayleigh waves along the East Pacific rise: evidence for S wave velocity anomalies to 450 km depth. *J. Geophys. Res.* 87, 8631–8641.
- Zhong, S., Davies, G.F., 1999. Effects of plate and slab viscosities on the geoid. *Earth Planet. Sci. Lett.* 170, 487–496.